JOURNAL OF AIRCRAFT
Vol. 34, No. 2, March–April 1997

Simulations of Turbulent Droplet Dispersion in Wind-Tunnel Icing Clouds

Brian C. DeAngelis* and Eric Loth†
University of Illinois at Urbana–Champaign, Urbana, Illinois 61801
and
Dennis Lankford‡ and C. Scott Bartlett‡
Sverdrup Technology, Inc., Arnold Air Force Base, Tennessee 37389

The objective of this study was to implement and test a computational methodology designed for robust and accurate prediction of spray-bar droplet dispersion for aeropropulsion icing tests. The three-dimensional methodology combines the NPARC code and a modified KIVA-II code (K-ICE). A validation study was completed to test the stochastic eddy model for turbulent dispersion calculations. Parametric studies were completed on an extracted domain slice of an NPARC air flowfield solution for an aeropropulsion test cell. The parametric studies tested the influence of computational, spray, vapor, and tunnel characteristics on liquid water content (LWC) spatial distribution. Results showed the strong sensitivity of LWC uniformity to turbulent kinetic energy, and initial droplet velocity and temperature. In addition, two calculations were performed on the full domain solution with two different nozzle spray arrangements. The predicted accretion patterns were similar to those found experimentally, although high-resolution simulations showed that LWC distributions at the test section can exhibit significant nonuniformity on small spatial scales.

Nomenclature

A = area
C_D = drag coefficient
c_μ = turbulent length scale coefficient = 0.09
D = Fick's law diffusion coefficient
$\boldsymbol{g}$ = gravity acceleration vector
k = turbulent kinetic energy
N_p = number of particles or droplets in a parcel
$\dot{N}_p$ = number parcels injected per second per nozzle
$\overline{n_p}$ = average number of parcels collected per bin
p = pressure
r = radius
T = temperature
t = time
t_e = eddy lifetime
t_f = collection time for LWC measurement
t_t = particle–eddy traversal time
t_{turb} = particle–eddy interaction time
$\boldsymbol{u}$ = velocity vector, $u\boldsymbol{i} + v\boldsymbol{j} + w\boldsymbol{k}$
$\boldsymbol{x}$ = position vector, $x\boldsymbol{i} + y\boldsymbol{j} + z\boldsymbol{k}$
$\overline{Y^2}$ = particle dispersion
Δt = time step
Δx = mesh size
$\Delta \boldsymbol{x}_p$ = particle or parcel position change
$\delta \boldsymbol{x}'_p$ = random position change
ε = turbulent dissipation
μ = viscosity
ν = kinematic viscosity
ρ = density
$\dot{\rho}^s$ = spray vapor source term
σ = LWC uniformity

Subscripts
air = air variable
i = injection variable
K-ICE = K-ICE (calibrated) value
KIVA-II = KIVA-II (uncalibrated) value
p = droplet, particle, or parcel variable
v = vapor variable
32 = Sauter mean variable

Superscripts
n = variable at time n
$'$ = fluctuating (turbulent) component variable
$\cdot$ = time rate of change of variable
$-$ = mean variable

Introduction

GROUND-BASED reproduction of cloud-induced icing conditions has taken on a consistent form. Whether the test facility is designed for propulsion testing, such as the Arnold Engineering and Development Center (AEDC) Engine Test Facility J-2 test cell,[1] or aerodynamic testing, such as the NASA Lewis Icing Research Tunnel,[2] water is typically sprayed by the nozzles of a system of spray-bars in an upstream portion of a dry air wind tunnel. In such designs, warm water is atomized by high-pressure air within each of the nozzles located at the trailing edge of the spray-bar. The resulting mist, composed of appropriately sized water droplets, is entrained by the moving tunnel air in the wake of the spray bars, where it goes into a supercooled state based on the subfreezing air temperatures. The supercooled microdroplets are then transported downstream and dispersed with the objective of forming a uniform droplet cloud within the test section to mimic atmospheric icing conditions.[3]

A primary design consideration of the ground-based icing cloud is the distribution and quantity of liquid water content

---

Received June 3, 1996; revision received Nov. 21, 1996; accepted for publication Nov. 22, 1996. This paper is declared a work of the U.S. Government and is not subject to copyright protection in the United States.

*Graduate Research Assistant, Aeronautical and Astronautical Engineering; currently Engineer, Boeing Co., Seattle, WA 98124. Member AIAA.

†Associate Professor, Aeronautical and Astronautical Engineering. Senior Member AIAA.

‡Senior Engineer, AEDC Group. Member AIAA.

(LWC) at the test section. LWC is defined as the mass of liquid water per unit volume of air, and its uniformity at the test section is considered a primary performance characteristic. Because trial-and-error adjustment of nozzles or test conditions can prove prohibitively expensive, computational methods have been proposed to numerically simulate the ground-based icing cloud by using a two-phase flow algorithm. Since turbulent dispersion can be an important means of achieving spatial uniformity, such physics should be properly accounted for by the algorithm.

The objective of this study was to develop an accurate and robust numerical algorithm for the modeling of the icing cloud flowfield of an icing wind tunnel with spray bars. The developed algorithm was used to quantify effects of the primary aerothermodynamic parameters on LWC uniformity to aid in designing future icing tunnels. This particular study focuses on modeling ground-based icing clouds in the AEDC Aeropropulsion Test Facility (ASTF). The results, however, are thought to be generally applicable to many spray-bar icing tunnels (aerodynamic and propulsion).

Numerical Methodology

Loth[4] proposed a computational strategy for the simulation of the flowfield in an icing wind tunnel. Because turbulence modulation and droplet effects on gas-phase momentum are negligible as a result of low overall droplet mass loading, the air-phase solution can be computed a priori with a single-phase internal flow solver. Therefore, the proposal involved a two-part scheme: 1) an airflow calculation followed 2) by droplet and vapor-phase calculations. The droplet and vapor phases can be calculated using a particle trajectory/species diffusion code. The trajectory portion computes turbulent dispersion by a stochastic eddy method, for which the air-phase solution provides turbulent energy and dissipation fields. Droplet collisions are ignored based on the highly dilute conditions of typical icing tunnels.

The two types of calculations were performed using two proven flow solvers in a sequential fashion. The fluid solver used for the airflow calculation was NPARC.[5] Whereas, all particle (solid or liquid droplets) and vapor calculations have been completed using a modified version of KIVA-II,[6] written at Los Alamos for internal combustion engine study. The modified version of KIVA-II used to investigate spray-bar configurations for icing conditions is referred to herein as K-ICE. Using the steady-state solutions of the airflow velocity, density, temperature, and turbulence quantities from NPARC, the water liquid and vapor phases are then computed with K-ICE. This architecture enables the more efficient use of computer time when parametric studies of different spray conditions for the same tunnel airflow conditions are to be completed. The following provides a brief overview of the governing equations for the vapor and particle phases in KIVA-II.

Vapor generated by the evaporation of droplets will have a negligible effect on the momentum of the air in the icing wind tunnel. This is because the vapor constitutes a very small fraction of the gas mass at low-temperature conditions. Therefore, there will be a one-way coupling of the air and vapor momentum. Using the spatially varying mean gas velocity $\bar{\boldsymbol{u}}$ and temperature T for the air and vapor provided from a three-dimensional NPARC calculation, the governing equation of the vapor density is given by the following:

$$\frac{\partial \rho_v}{\partial t} + \nabla \cdot (\rho_v \bar{\boldsymbol{u}}) = \nabla \cdot \left[\rho D \nabla \left(\frac{\rho_v}{\rho} \right) \right] + \dot{\rho}^s \tag{1}$$

where ρ_v is the partial vapor density (the fraction of gas density that is attributable to water vapor) and ρ is the total gas density. The equation is solved by the finite volume method and an arbitrary Lagrangian–Eulerian (ALE) scheme of KIVA-II.[6]

Particle (or droplet) movement is dictated by the coupling of two equations of motion. The particle trajectory is governed by the following:

$$\frac{\mathrm{d}\boldsymbol{x}_p}{\mathrm{d}t} = \boldsymbol{u}_p \tag{2}$$

where $\boldsymbol{x}_p$ is the particle location and $\boldsymbol{u}_p$ is the particle velocity. The particle acceleration is affected by only aerodynamic drag and gravity if the particle density is much greater than the gas density ($\rho_p >> \rho$).[7] Thus, the particle velocity can be found by solving a standard equation of motion for a spherical droplet of r_p

$$\frac{\mathrm{d}\boldsymbol{u}_p}{\mathrm{d}t} = \frac{3}{8} \frac{\rho}{\rho_p} \frac{|\bar{\boldsymbol{u}} + \boldsymbol{u}' - \boldsymbol{u}_p|}{r_p} (\bar{\boldsymbol{u}} + \boldsymbol{u}' - \boldsymbol{u}_p) C_D + \boldsymbol{g} \tag{3}$$

where $\boldsymbol{u}'$ is the fluctuating component of the gas velocity. Because all particles are considered spherical, C_D is taken to be

$$\begin{aligned} C_D &= (24/Re_p)[1 + (Re_p^{2/3}/6)] \qquad Re_p \leq 1000 \\ &= 0.424 \qquad\qquad\qquad\qquad\quad Re_p > 1000 \end{aligned} \tag{4}$$

where

$$Re_p = \frac{2\rho |\bar{\boldsymbol{u}} + \boldsymbol{u}' - \boldsymbol{u}_p| r_p}{\mu(\hat{T})} \tag{5}$$

$$\hat{T} = (T + 2T_p)/3 \tag{6}$$

where T_p is the particle temperature. Droplets will experience radius change caused by evaporation, the rate of which is dictated by the Frossling correlation outlined in Ref. 6. This contributes to the spray vapor source term of Eq. (1).

A single value of $\boldsymbol{u}'$ is used for each particle when that particle is within a given eddy. It is a random value that follows a Gaussian distribution with a standard deviation of $\sqrt{2k/3}$. When the particle enters an eddy, $\boldsymbol{u}'$ is chosen and the particle will experience this velocity for an approximate period of time called t_{turb}. This time is the minimum of either t_e or t_t, for example, in KIVA-II the following expression is used:

$$t_{\text{turb}} = \min(t_e, t_t) = \min \left(\frac{k}{\varepsilon}, \frac{c_\mu^{3/4} k^{3/2}}{\varepsilon} \frac{1}{|\bar{\boldsymbol{u}} + \boldsymbol{u}' - \boldsymbol{u}_p|} \right) \tag{7}$$

where c_μ is equal to 0.09.

Based on the previous discussion, the value $\boldsymbol{u}_p^n$ is found by using a finite difference approximation to Eq. (3). The calculation of particle trajectories is then completed by solving the Lagrangian finite difference approximation to Eq. (2). This is

$$\boldsymbol{x}_p^{n+1} = \boldsymbol{x}_p^n + \Delta t \boldsymbol{u}_p^n + \delta \boldsymbol{x}_p' \tag{8}$$

Note that in this equation, the subscript p now refers to parcels rather than particles. Each parcel represents N_p particles, all with identical properties. In the previous equation, $\delta \boldsymbol{x}_p'$ is a random position change chosen from a prescribed distribution based on $\boldsymbol{u}_p^n$, and is nonzero only when $\Delta t > t_{\text{turb}}$, as discussed in Ref. 6.

Validation

NPARC has been the subject of extensive validation,[8] which was important since no measurements of flow characteristics of the ASTF tunnel are available for comparison with the predictions. K-ICE was validated with results from a solid particle dispersion experiment. Although evaporation effects were not considered in these dispersion calculations, the validation allows critical investigation of the ability to predict turbulent diffusivity, a critical mechanism to predicting LWC distribution. Therefore, it is important to quantify the robustness of the stochastic eddy model for conditions similar to those experienced in icing tunnels.

Snyder and Lumley[9] performed particle dispersion measurements in a vertical wind tunnel. The turbulence was generated by the presence of a grid of mesh size 2.54 cm at an upstream portion of the tunnel ($z = 0$). Four particle types were studied. All flow variables, including k and ε, were measured or derived and expressed as functions of the tunnel axial position z. There were no variations of conditions in the x or y directions and gravity acted in the negative z direction. The time-averaged air velocity in the downstream direction $\bar{w}$ was measured at 655 cm/s with no mean velocity components in the lateral directions, i.e., $\bar{u} = \bar{v} = 0$. The data set has been used successfully in many particle code validation cases,[8] including Gosman and Ioannides[10] and Shuen et al.[11]

Because all flow variables were measured and presented by Snyder and Lumley,[9] an NPARC calculation as an input to K-ICE was not necessary for this study. All required flow variables were assigned to an appropriate grid. The values for k and ε were assigned directly based on the particle z position to eliminate the influence of the grid spacing in the calculation of turbulent dispersion.

Four types of particles, initialized by their radius and density, were injected along the centerline with velocity $w_p = 655$ cm/s at $z = 50.8$ cm. Turbulent dispersion was quantified by measuring the mean-square of lateral movement $\overline{Y^2}$ of each particle from an initial position at $z = 172.72$ cm. The time of crossing this z position was defined as zero seconds. For the numerical simulations, 800 particles were used in each case, as compared to approximately 700 particles used experimentally.

Large errors in predicted dispersion were found when using the original definitions for the eddy interaction time provided by KIVA-II. There was much more dispersion calculated than was measured by Snyder and Lumley[9] (note KIVA-II had not previously been directly validated against turbulent dispersion data). Shuen et al.[11] noted that because of somewhat arbitrary definitions of eddy length and time scales, such stochastic models typically require calibration. Modifying t_e and t_t, originally included in KIVA-II, led to increased accuracy. Therefore, with respect to the Snyder and Lumley data,[9] the new eddy interaction time $t_{\text{turb}_{\text{K-ICE}}}$ is the minimum of either

$$t_{e_{\text{K-ICE}}} = 0.20 t_{e_{\text{KIVA-II}}} = 0.20(k/\varepsilon) \tag{9}$$

$$t_{t_{\text{K-ICE}}} = 1.4 t_{t_{\text{KIVA-II}}} = 1.4 \frac{c_\mu^{3/4} k^{3/2}}{\varepsilon} \frac{1}{|\bar{\boldsymbol{u}} + \boldsymbol{u}' - \boldsymbol{u}_p|} \tag{10}$$

Note that other studies have used similar coefficients for t_e, such as 0.235 (e.g., Lu et al.[12]) and 0.201 (e.g., Shuen et al.[11]).

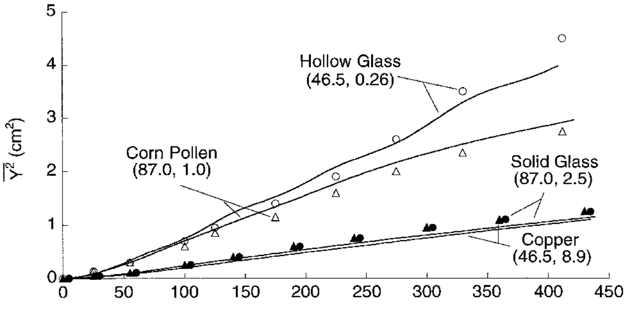

Fig. 1 Particle dispersion as a function of time for the Snyder and Lumley[9] experiment shown with symbols and with particle diameter and density in parentheses given in units of μm and g/cm^3, respectively. Present predicted values of K-ICE shown with solid lines.

For the modified time scales, results for the four particle types in terms of $\overline{Y^2}$ are shown in Fig. 1. Across the range of particle densities and sizes, dispersion is modeled fairly accurately for all times. Typically, the dispersion of the heavier particles were dominated by the transit time, whereas the lighter particles were dominated by the eddy lifetime. Note that icing simulations use water droplets with approximately the same density as corn pollen, and which traverse the flowfield in less than 100 ms. Therefore, the droplets are more likley to be dispersed by eddy lifetime mechanisms.

Test Conditions

This study sought to model a typical AEDC ASTF icing test cell condition; specifically, a test section Mach number of 0.4 with a static pressure of approximately 0.5 atm and a static temperature of approximately 261 K. Only a quarter-section computation of the ASTF flowfield was computed with NPARC because of spray-bar and tunnel symmetry. The NPARC solution for streamwise velocity $\bar{w}$ in the $y = 0$ plane is shown in Fig. 2. Flow direction is left to right. Note the spatial nonuniformities caused by the spray-bar wakes at the far upstream portion of this figure.

Two separate studies were conducted with K-ICE using this single ASTF air flowfield solution. The first study included a series of parametric tests using an extracted slice of the one-quarter domain solution, which incorporated flow between two spray bars extending from the center of the tunnel to the wall. The spray nozzles were placed according to actual geometries and several varying conditions were run to witness the effects of parameter changes on the flowfield. In the second study, the complete one-quarter domain was used for computations for two different nozzle spray arrangements. Both studies are described next.

Parametric Studies on an Extracted Slice Domain

A slice of the computational domain and NPARC gas-phase solution for the ASTF wind tunnel was extracted and used as a test section for various computational and physical parameter variation studies of droplet dispersion. This reduced three-dimensional computational domain was used to allow several parameter variations without requiring the excessive computational resources of the one-quarter section three-dimensional simulations. The extracted region was chosen based on all grid points within an area between the midline of the first and second spray bars. Figure 3 is a schematic diagram of the quarter-section of the test cell that was solved with NPARC and shows the small section that was extracted to provide the grid of the partial domain. The number of vertices in each direction that form the partial extracted domain are identified. Also in this figure is the spray-bar arrangement for the tunnel quarter section with an enlarged view of the two spray bars within the extracted region. The slice in the x–y plane (indicated by the

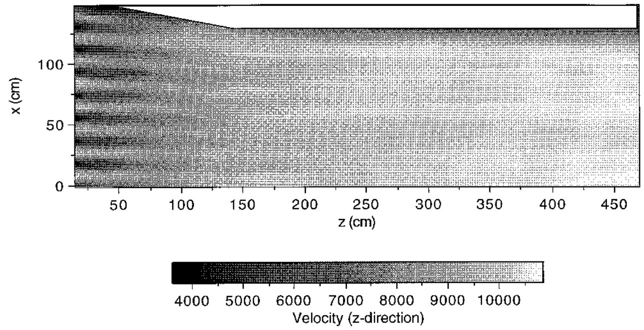

Fig. 2 Gray-scale distribution of axial velocity, *w* (cm/s) in the center vertical plane of the one-quarter domain ASTF flowfield as computed by NPARC. Black corresponds to the minimum value of 3600 cm/s and white corresponds to the maximum value of 10,800 cm/s.

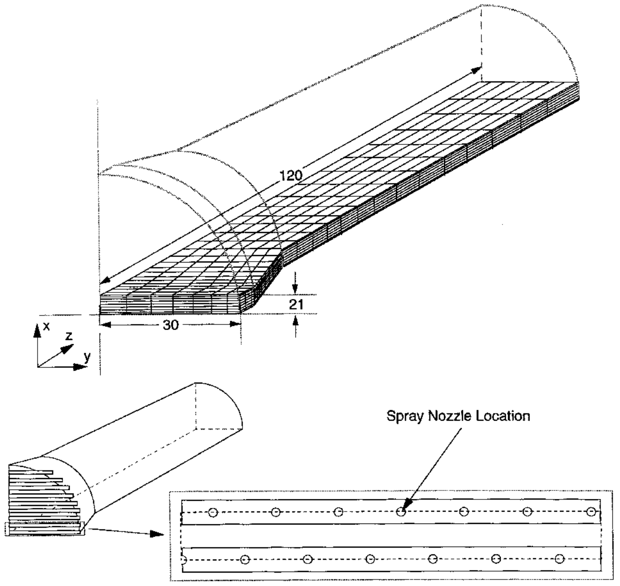

Fig. 3 Schematic diagram of the quarter-section of the test cell that was solved with NPARC and the small section that was used to provide the grid of the extracted slice domain. A close-up of the spray bar-nozzle configuration of the extracted grid is also shown.

region within the dashed lines) was made to include two half-rows of nozzles. Note that the nozzles spray from the downwind side of the spray bars in the positive z direction. Actual nozzles were configured in the staggered fashion as shown in Fig. 3, spraying in a hollow cone with an included angle of 70 deg and a secondary spray angle of 12 deg, simulating the hollow cone atomizer used in the ASTF test cell.

Several tests were conducted using the extracted flowfield and appropriate boundary conditions. These droplet boundary conditions assumed that all computational boundaries except the inflow and outflow were treated as reflective tunnel walls, i.e., the particles hitting these boundaries were bounced elastically. This condition was employed because the extracted grid boundaries were always nearly coincident to the streamlines of the flowfield and because spray-bar symmetry was assumed in the x and y directions. In addition, changing to a stick condition at the boundaries, which coincided with tunnel walls, yielded a negligible effect on mean LWC or its uniformity. A baseline case (case 0) and four sets of computations were completed with K-ICE. Except for the identified parameter or assumption investigated for each case, the different cases described next had the same characteristics as the baseline case (see Table 1):

1) Computational parameters to investigate numerical sensitivities with respect to a, $\dot{N}_p$; b, Δt; and c, t_{turb}.

2) Computational assumptions with regard to droplet evaporation: a, nonuniform vapor pressure distribution p_v, i.e., inclusion of water vapor convection/diffusion along with droplet trajectories; and b, negligible evaporation $\dot{r}_p$, i.e., no evaporation or vapor convection/diffusion.

3) Droplet parameters to investigate sensitivity to changes in a, injected droplet Sauter mean radius $r_{p_{32i}}$; b, $|\boldsymbol{u}_{p_i}|$; and c, droplet injection temperature T_{p_i}.

4) Tunnel conditions to study sensitivity because of air flowfield changes in a, tunnel mean static temperature T, p constant; b, tunnel mean static pressure p, T constant; and c, tunnel turbulence as a percent of the computed turbulent kinetic energy k/k_{NPARC}.

Each of these cases is identified by the number and letter just specified. Injected values are given a subscript i. The varied values for all cases can be seen in Table 2.

Table 1 Baseline case computational parameters and flow conditions

Variable	Value
$\dot{N}_p$	40,000 parcels/nozzle/s
Δt	0.12 ms
t_{turb}	$t_{\mathrm{turb}_{\mathrm{K\text{-}ICE}}}$
p_v	0 (everywhere)
$\dot{r}_p$	based on p_v
$r_{p_{32i}}$	10 μm
$\lvert\boldsymbol{u}_{p_i}\rvert$	5000 cm/s
T_{p_i}	300 K
T	273 K
p	0.5 atm
k/k_{NPARC}	100%

Table 2 Varied computational parameters and flow conditions for extracted slice domain

Case	Variable	Value
1a	$\dot{N}_p$	20,000 parcels/nozzle/s
1b	Δt	0.24 ms
1c	t_{turb}	$t_{\mathrm{turb}_{\mathrm{KIVA\text{-}II}}}$
2a	p_v	Nonuniform
2b	$\dot{r}_p$	0
3a	$r_{p_{32i}}$	25 μm
3b	$\lvert\boldsymbol{u}_{p_i}\rvert$	2500 cm/s
3c	T_{p_i}	310 K
4a	T	249 K
4b	p	0.33 atm
4c	k/k_{NPARC}	80%

Specific values for the parameters were chosen based on several constraints. For the baseline case, the maximum computational accuracy was desired, whereas the variation cases tested less computationally intensive conditions for assessment of error and cost savings. Some parameter values represent conditions for different experimental test cases. Other values were chosen to help estimate influence of experimental or NPARC numerical uncertainty with respect to mean LWC and its uniformity.

Two of the tests warrant more detailed comments. To test whether computation of the water vapor spatial distribution was important, case 2a was considered where the vapor field was fully simulated. The results were then compared to the baseline case where the vapor field was simply taken to be uniformly negligible ($p_v = 0$). Note that the tunnel temperatures for this comparison were at the maximum value for which icing tunnels might be expected to operate to test the vapor elimination assumption for an extreme condition. It will be seen later that the assumption of $p_v = 0$ is very reasonable for these types of flows, allowing for significantly reduced computational costs in the remaining parametric cases. A second test case to describe further is that of 2b, for which the vapor field is considered to be saturated everywhere, such that droplet evaporation will be negligible ($\dot{r}_p = 0$).

For each of the 12 cases (one baseline and 11 variations), droplets were injected (in the form of parcels) from the nozzle locations at a mass flow rate per nozzle of 3.91 g/s starting at $t = 0$. The droplets were continuously injected, tracked, and convected out of the domain until the flowfield reached a statistically steady state. Temporal evolution of liquid mass flux and LWC profiles were then determined at six downstream planes, numbered 1–6, located approximately 10, 25, 50, 100, 200, and 400 cm, respectively, from the nozzle plane z location. For the LWC profiles, each plane was divided into 210 equally sized square bins (matrix of 42 × 5). If a particle passed through a bin, data for the calculation of LWC [see Eq. (9)] were stored. For each bin, the sum of m_p/w_p for all par-

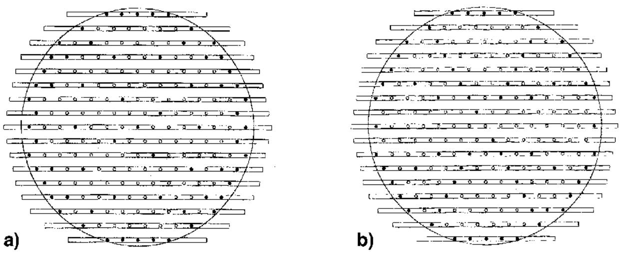

Fig. 4 Schematic of ASTF spray a) solid-pattern and b) X-pattern (both facing upstream). Hollow circles indicate operational nozzles and solid circles indicate plugged (nonoperational) nozzles.

ticles passing through in time increments of t_f (corresponding to 0.06 s) was recorded.

Simulations on a One-Quarter Domain

Based on computations described in the previous section, two calculations were performed to reproduce the LWC in the full ASTF test section. The various parameters used for the calculations are the same as in the baseline case of Table 1, except that $\Delta t = 0.24$ ms (to effectively reduce CPU time) and $T = 261$ K (to correspond to experimental conditions). The two calculations are based on two nozzle spray arrangements that have been used to generate actual icing clouds. These arrangements (known as the solid-pattern case and the X-pattern case) are shown in Figs. 4a and 4b. Individual nozzle characteristics (including mass flow rate) and injector spacing were the same as used in the previous section. All particles impacting walls (either symmetry or physical walls) were considered elastic collisions. To maintain the same bin physical dimensions, a large increase in the total number of bins was required (as compared to the extracted case) to collect LWC data at the same six streamwise locations as before. Even though the gas flowfield computed with NPARC is quarterly symmetric, the X-pattern case nozzle pattern is not. Therefore, two separate K-ICE calculations were performed independently of each other on two different quarter-sections and then assembled to present the spray in the full domain. Though this type of modeling is not as accurate as a half-domain calculation, it is much less computationally intensive, and errors should only occur near quarter-section interfaces.

Results and Discussion

Parametric Studies on an Extracted Slice Domain

Baseline and other case results are shown in Figs. 5–7 and are discussed first. Figure 5 is a typical instantaneous profile of all the particle locations in the horizontal y–z plane. Note the hollow-cone spray (issuing from the left) is diffused in the downstream portions of the domain. Figure 6 shows the baseline time evolution (shaded plot) of the normalized LWC at plane 6, where each frame indicates a time average over 500 time steps. Here, only small fluctuations are noted between the later time of 2000–2500 time steps, where the solution can be considered converged. The steady-state result shows a reduced LWC near the wall (right-hand side of computational domain), which is consistent with results of Bragg and Khodadoust.[13] Figure 7 is a time-averaged vapor profile along a y–z plane near the bottom row of injectors for case 2a, where white indicates maximum vapor level and black indicates an absence of vapor. The continual transverse diffusion of vapor as the flow convects to the right is clearly seen. However, even at the exit, these variations have not been completely eliminated.

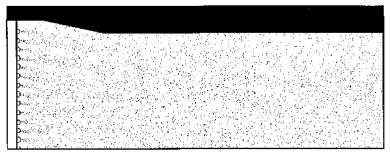

Fig. 5 Instantaneous parcel distribution in the extracted slice domain of the ASTF flowfield for baseline case with nozzle locations indicated on left-hand side.

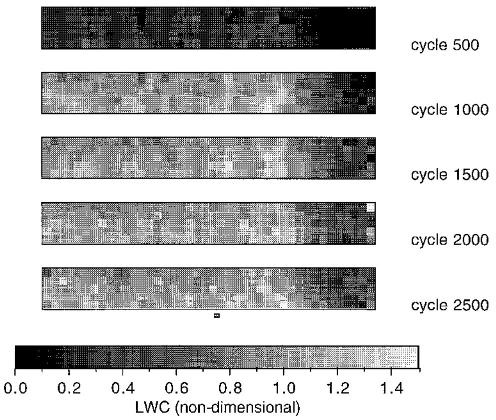

Fig. 6 Temporal evolution of spatial LWC (gray-scale) distribution normalized by peak value (1.152 μg/cm^3) in the extracted slice domain for the baseline case, where every 500 cycles represents 60 ms. Black corresponds to an LWC of zero and white corresponds to an LWC of 1.5 times the spatially averaged mean value of the converged solution.

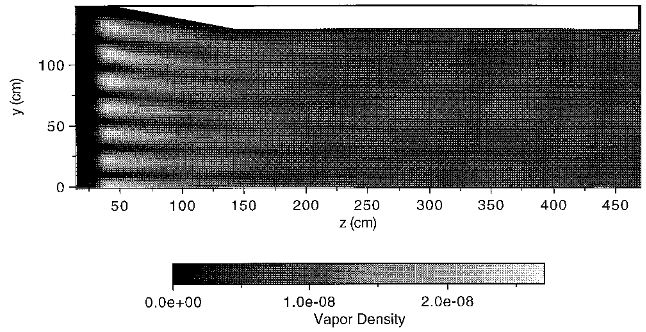

Fig. 7 Gray-scale distribution of time-averaged vapor distribution ρ_v (g/cm^3) at a y–z plane near the bottom row of injectors in the extracted slice domain for case 2a. Black corresponds to a vapor density of zero and white corresponds to a vapor density of 2.7×10^{-8} g/cm^3.

Several global characteristics were calculated to characterize the computational flowfield and are summarized in Table 3 along with the computational requirements. For each case, the varied parameter value is shown, along with $\overline{\text{LWC}}$ (the overall mean LWC averaged over the plane 6 area and the 0.30 s from $t = 0.18$ to 0.48 s), and σ (the standard deviation of the converged time-averaged spatial distribution from the overall mean). The standard deviation is defined as

$$\sigma = \sqrt{\sum_{i=1}^{n} (\text{LWC}_i - \overline{\text{LWC}})^2/(n - 1)} \tag{11}$$

where LWC_i is equal to the local time-averaged LWC at bin i and n is the total number of bins (210). The standard deviation is a measure of the LWC uniformity, i.e., the lower the standard deviation, the more uniform the LWC. Alternately, higher σ refers to more nonuniformity. In Table 3, $\overline{\text{LWC}}$ and σ are both normalized by the $\overline{\text{LWC}}$ of case 2b (the no-droplet evaporation case).

Computationally, several trends can be noted from Table 3. A 50% drop in the parcels (and thus computational matrix size) translates to a 50% reduction in CPU time. Several other res-

Table 3 Statistical results for extracted slice domain calculation

Case description		LWC data (plane 6)		Computer resources	
Case	Varied parameter	$\overline{\text{LWC}}$	σ	Memory, MWords	CPU time,[a] h
0	See Table 1	0.909	0.233	2.2	0.727
1a	$\dot{N}_p = 20{,}000$ p/s/n	0.904	0.247	2.1	0.375
1b	$\Delta t = 0.24$ ms	0.900	0.236	2.2	0.416
1c	$t_{\text{turb}} = t_{\text{turb}_{\text{KIVA-II}}}$	0.928	0.179	2.2	0.751
2a	p_v = nonuniform	0.900	0.238	7.0	2.204
2b	$\dot{r}_p = 0$	1.000	0.238	2.2	0.496
3a	$r_{p_{32i}} = 25$ μm	0.989	0.229	2.2	0.800
3b	$\lvert \boldsymbol{u}_{p_i} \rvert = 2500$ cm/s	0.906	0.248	2.2	0.766
3c	$T_{p_i} = 310$ K	0.844	0.215	2.2	0.755
4a	$T = 249$ K	0.971	0.235	2.2	0.727
4b	$p = 0.33$ atm	0.888	0.228	2.2	0.726
4c	$k/k_{\text{NPARC}} = 80\%$	0.910	0.267	2.2	0.739

[a] Based on a Cray C-90 operating at ~30 MFlops for the particle and evaporation routines.

olution tests were run to confirm the sensitivity of statistics on the average number of parcels collected per bin $\overline{n_p}$. The results are consistent with uncertainty scaling with $1/\sqrt{\overline{n_p}}$, as suggested by conventional ergodic statistics. Convergence to within 1% of $\overline{\text{LWC}}$ was achieved with $\overline{n_p} \approx 385$, corresponding to the baseline case of 40,000 parcels injected per second per nozzle.

As seen in Table 3, the negligible sensitivity of including the full water-vapor convection and diffusion (case 2a) suggests that predicting local vapor concentration (as opposed to assuming it is zero everywhere) is not necessary. This is consistent with the maximum vapor pressure resulting from evaporation (based on Fig. 7) being several orders of magnitude less than the saturated vapor pressure at $T = 273$ K. Therefore, while the evaporation calculation is critical for obtaining the correct value of $\overline{\text{LWC}}$ and a slightly more accurate value of σ (as compared to case 2b), the vapor convection and diffusion calculations, required to predict a nonzero vapor distribution, have little effect on the results. This is important in that the vapor computation consumes the majority of the computational resources for such a calculation, as indicated by a nearly 300% increase in CPU time and memory for case 2a.

Also seen from Table 3, the three most crucial physical parameters affecting σ are droplet initial velocity, initial droplet temperature, and tunnel turbulence. The first result (case 3b) yields higher σ for a doubling of $\lvert \boldsymbol{u}_{p_i} \rvert$ is because of decreased inertia of the droplets at injection, spreading the droplets less effectively from the nozzle origin and creating less uniformity. The second result (case 3c) shows a lower σ for a 10-deg increase in T_{p_i} and is caused by the increased droplet evaporation after droplets have already been spread by the nozzle, resulting in smaller droplets with smaller Stokes numbers that can diffuse more effectively. The third result (case 4c) shows a 20% decrease in turbulent kinetic energy can significantly reduce σ and is because of the subsequent reduced turbulent dispersion of the droplets. Another crucial physical parameter affecting σ is droplet injection radius (case 3a), though it is not completely evident by the results listed in Table 3. In a previous study, when original KIVA-II turbulent time scales were considered (causing greater dispersion), the increasing droplet size tended to decrease the uniformity since the larger Stokes number droplets were unable to disperse as quickly and tended to simply follow the mean flow. In another previous study, when decreased turbulent eddy interaction times were considered, increasing droplet size tended to increase the uniformity, because of the domination of the initial spray inertia in dispersing droplets. Thus, in the current study, the increasing droplet size coincidentally did not influence the uniformity because of the counteractive effects, but, in general, its influence can be significant.

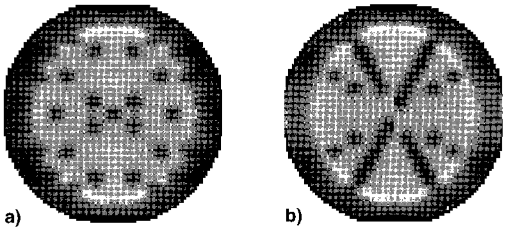

Fig. 8 Gray-scale distribution of cross-sectional LWC at axial plane 6 for a) solid-pattern case and b) X-pattern spray case. Black corresponds to an LWC of zero and white corresponds to an LWC of 1.5 times the spatially averaged mean value of the converged solution.

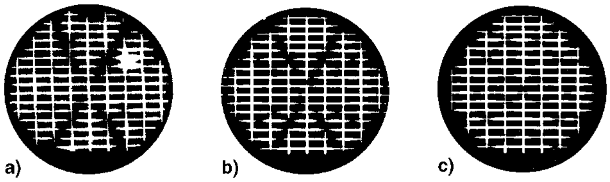

Fig. 9 Digitized images of ice accretion at plane 6 based on a) photograph of experiments using collection pipes of the X-pattern spray case, b) simulation of X-pattern spray case, and c) simulation of solid-pattern spray case. The simulated accretion is represented by the local thickness of white lines that coincide with the experimental collection pipe locations.

Simulations on a One-Quarter Domain

The LWC distributions at plane 6 of both the solid-pattern case and X-pattern case are shown in Figs. 8a and 8b, normalized by the same value as in the parametric study. In each plot, the sections (a single quarter-section for the solid-pattern and two different quarter-sections for the X-pattern) are pieced together and arranged to produce a full ASTF test cell cross section. The solid-pattern case is characterized by a fairly uniform LWC distribution, except for around the tunnel walls and at several locations inside the cross section where low LWC regions (holes) are located. These holes correspond to locations where nozzles were not used (see Fig. 4a). The X-pattern case exhibits many of the same characteristics, with additional LWC holes corresponding to locations of nozzles not in use (see Fig. 4b). In this case, the pattern of the X in the nozzle configuration is clearly evident, with a secondary pattern of low LWC showing at the left and right of the X.

To investigate the fidelity of the simulation, the X-pattern case is compared against a digitized image of a photograph of ice accretion on a series of pipes arranged across the ASTF test section in an actual experimental test of the X-pattern (see Fig. 9a). The digitized image tends to color all locations with photographed ice as white and all other structures as black. The large white region in the upper-right portion of the image is the result of a faulty nozzle that sprayed a continuous water stream down the tunnel length. Note that the region at the very bottom of the image (lowest spray bar) was set to black to eliminate some digitization errors. Since the circumference of the accreted ice can be approximated as linearly proportional to LWC (Ref. 3), and the diameter is linearly related to the circumference, the thickness of the white regions in Fig. 9a (which is the accreted ice diameter), can thus be approximately linearly related to LWC.

To simulate the digitized photograph of Fig. 9a using calculated LWC results, data were extracted from the X-pattern results only in regions where pipes are located in the photograph. The resulting LWC was numerically smoothed over a length scale consistent with the experimental pipe diameter. The simulated accretion (Fig. 9b) is then represented by the local thickness (based on local LWC) of white lines, which coincide with the experimental collection pipe locations. Since the collection efficiency of the icing pipes was not known, the total simulated ice accretion (as measured by fraction of the image that is white) was adjusted to match the total experimental ice accretion (excluding the accretion from the faulty experimental nozzle). Note that the LWC in the region at the very bottom part of the plot was set to zero to match the same correction made to the digitized photograph when the lower portion was set to black.

The processed image in Fig. 9b shows strong similarity to the digitized photograph of Fig. 9a, though it is unclear as to the extent that the two images can be correlated, for example, the digitized experimental accretion is not necessarily linearly proportional to LWC, and the calculation may contain errors because of uncertainty in turbulent dispersion. Qualitatively, however, both the computed and photographed ice accretion patterns resemble each other significantly. It is important to note that neither image clearly shows the detailed structures present in the higher resolution pattern of Fig. 8b. This indicates how the loss in measurement resolution significantly alters the perceived structure of the LWC.

Figure 9c is a processed image of the LWC levels of the solid-pattern case in the regions where accretion pipes would be located. The image was produced in the same fashion as the image of Fig. 9b. While this compares well with experiment, as before, the comparison is largely qualitative. It is again important to note that this figure is in contrast to the corresponding solid-pattern LWC profile structure of Fig. 8a where deviations in the LWC are more apparent than in the processed image of Fig. 9c. Thus, Fig. 9c gives the appearance of fairly uniform LWC in the majority of the center portion of the domain.

Conclusions

Several conclusions were derived from the study. Through parametric studies, the present numerical scheme proved to be efficient in computing liquid water content (LWC) distributions for complex geometries. Fortunately, the icing tunnel regime allows one to simplify the physics that need to be modeled, most importantly that we may neglect the spatial variations in vapor distribution, the calculation of which causes a substantial increase in computational cost. While less turbulence is often a desired feature of wind tunnels, it has been shown that increasing tunnel turbulence levels can be an effective means of creating LWC uniformity. Aside from tunnel conditions, initial droplet conditions have also proven to be instrumental in changing the uniformity. Larger droplets and higher injection velocities seem to provide greater uniformity, though there may be a limit imposed by proper cloud droplet sizes and nozzle design. It was also shown that proper statistical sampling is necessary to provide converged characteristics of the LWC.

Employing the results of the parametric studies, two separate LWC calculations were made for a full test cell domain with optimal computational parameters and proper flow and droplet conditions. In one case, the *X*-pattern case, a digitized image of a photograph of ice accretion on pipes in the test section was used to determine physical accuracy of the computation. Using a process that changed computed LWC data into equivalent ice thickness where pipes existed in the experiment, an image was produced that has a strong similarity to the digitized photograph. However, the simulated ice thickness images (which were diffused to give a resolution consistent with that of the experiment), failed to reveal significant small-scale deviations in LWC when compared to the high spatial resolution calculations. This indicates that high resolution may be critical for accurate judgment of LWC uniformity.

Acknowledgments

This work was supported by the Arnold Engineering Development Center, Sverdrup Technology, Inc., and the Air Force Office of Scientific Research. Computer time was furnished by the National Center for Supercomputing Applications and the Pittsburgh Supercomputing Center.

References

[1] DeAngelis, B. C., "Computations of Turbulent Droplet Dispersion for Wind Tunnel Icing Tests," M.S. Thesis, Univ. of Illinois at Urbana–Champaign, IL, 1996.

[2] Bartlett, C. S., and Phares, W. J., "Icing Testing of a Large Full-Scale Inlet at the Arnold Engineering Development Center," AIAA Paper 93-0299, Jan. 1993.

[3] Ide, R. F., "Liquid Water Content and Droplet Size Calibration of the NASA Lewis Icing Research Tunnel," AIAA Paper 90-0669, Jan. 1990.

[4] Loth, E., "Computational Methodology for Wind Tunnel Spray Bar Droplet Dispersion," AFOSR Summer Research Program, Final Rept., Aug. 1993.

[5] Cooper, G. K., and Sirbaugh, J. R., "PARC Code: Theory and Usage," Arnold Engineering and Development Center, TR 89-15, Arnold AFB, TN, Jan. 1989.

[6] Amsden, A. A., O'Rourke, P. J., and Butler, T. D., "KIVA-II: A Computer Program for Chemically Reactive Flows with Sprays," Los Alamos National Lab., DE89-012805, Los Alamos, NM, May 1989.

[7] Towne, C. E., and Jones, R. R., "Results and Current Status of the NPARC Alliance Validation Effort," AIAA Paper 96-0387, Jan. 1996.

[8] Kuo, K. K., *Principles of Combustion*, Wiley, New York, 1986, p. 582.

[9] Snyder, W. H., and Lumley, J. L., "Some Measurements of Particle Velocity Autocorrelation Functions in a Turbulent Flow," *Journal of Fluid Mechanics*, Vol. 48, Pt. 1, 1971, pp. 41–71.

[10] Gosman, A. D., and Ioannides, E., "Aspects of Computer Simulation of Liquid-Fuelled Combustors," AIAA Paper 81-0323, Jan. 1981.

[11] Shuen, J.-S., Chen, L.-D., and Faeth, G. M., "Evaluation of a Stochastic Model of Particle Dispersion in a Turbulent Round Jet," *Journal of the American Institute of Chemical Engineers*, Vol. 29, No. 1, 1983, pp. 167–170.

[12] Lu, Q. Q., Fontaine, J. R., and Aubertin, G., "Numerical Study of the Solid Particle Motion in Grid-Generated Turbulent Flows," *International Journal of Heat and Mass Transfer*, Vol. 36, No. 1, 1993, pp. 79–87.

[13] Bragg, M. B., and Khoudadoust, A., "Study of the Droplet Spray Characteristics of a Subsonic Wind Tunnel," *Journal of Aircraft*, Vol. 32, No. 1, 1995, pp. 199–207.